JACS JOURNAL OF THE AMERICAN CHEMICAL SOCIETY

Article

Cite This: J. Am. Chem. Soc. 2017, 139, 14425-14435

pubs.acs.org/JACS

Tuning Product Selectivity for Aqueous CO_2 Reduction with a Mn(bipyridine)-pyrene Catalyst Immobilized on a Carbon Nanotube Electrode

Bertrand Reuillard,[†,‡] Khoa H. Ly,[†,‡] Timothy E. Rosser,[†] Moritz F. Kuehnel,[†] Ingo Zebger,[§] and Erwin Reisner*[,†]

[†]Christian Doppler Laboratory for Sustainable SynGas Chemistry, Department of Chemistry, University of Cambridge, Lensfield Road, Cambridge CB2 1EW, United Kingdom

[§]Max Volmer Laboratorium für Biophysikalische Chemie, Sekretariat PC14, Institut für Chemie, Technische Universität Berlin, Straße des 17. Juni 135, 10623 Berlin, Germany

Supporting Information

ABSTRACT: The development of high-performance electrocatalytic systems for the controlled reduction of CO_2 to value-added chemicals is a key goal in emerging renewable energy technologies. The lack of selective and scalable catalysts in aqueous solution currently hampers the implementation of such a process. Here, the assembly of a [MnBr(2,2′-bipyridine)$(CO)_3$] complex anchored to a carbon nanotube electrode via a pyrene unit is reported. Immobilization of the molecular catalyst allows electrocatalytic reduction of CO_2 under fully aqueous conditions with a catalytic onset overpotential of η = 360 mV, and controlled potential electrolysis generated more than 1000 turnovers at η = 550 mV. The product selectivity can be tuned by alteration of the catalyst loading on the nanotube surface. CO was observed as the main product at high catalyst loadings, whereas formate was the dominant CO_2 reduction product at low catalyst loadings. Using UV−vis and surface-sensitive IR spectroelectrochemical techniques, two different intermediates were identified as responsible for the change in selectivity of the heterogenized Mn catalyst. The formation of a dimeric Mn^0 species at higher surface loading was shown to preferentially lead to CO formation, whereas at lower surface loading the electrochemical generation of a monomeric Mn-hydride is suggested to greatly enhance the production of formate. These results emphasize the advantages of integrating molecular catalysts onto electrode surfaces for enhancing catalytic activity while allowing excellent control and a deeper understanding of the catalytic mechanisms.

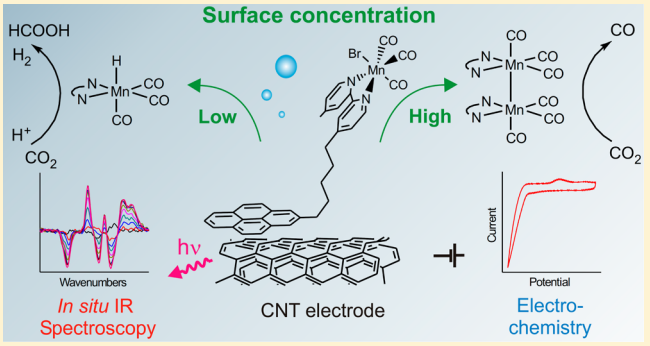

INTRODUCTION

Efficient, low-cost, and scalable electrocatalytic reduction of CO_2 is currently under consideration as a viable means to produce useful chemicals while limiting the rise of CO_2 levels in the atmosphere.[1−5] During the past few years, transition metal complexes have been extensively studied for the electro- and photoreduction of CO_2, mainly to carbon monoxide (CO) and formate ($HCOO^-$).[6−9] The molecular nature of these complexes allows specific fine-tuning of their structure using synthetic chemistry to rationally control the activity,[10] selectivity,[11] and stability of the catalysts via a profound understanding of the catalytic mechanisms involved.[12,13] In order to replace expensive Re,[14−17] Ru,[18,19] and Ir[20] based catalysts, a range of different catalytic structures incorporating more abundant first-row transition metals such as Ni,[21−23] Co,[24−27] Fe,[28,29] and Mn[30−32] have been described for catalytic CO_2 reduction.

The integration of these molecular species onto electrodes in many cases gives an enhancement of the catalytic activity and provides new insights into the involved mechanisms.[33−36] Immobilization also enables catalysts that would otherwise be insoluble to operate in water and overcomes limitations from diffusion-controlled electrocatalysis with catalysts in the bulk solution.[37−41] In this respect, carbon nanotubes (CNTs) are an established platform for the immobilization of molecular electrocatalysts.[42−45] Their high surface area and excellent conductivity allow grafting of large amounts of electrocatalytically active species while retaining good electron transfer properties.[46] The possibility to chemically modify CNTs using a variety of covalent or noncovalent techniques is another advantage of these nano-objects.[47] Specifically, the immobilization of pyrene-modified catalysts via $\pi-\pi$ interactions with the CNT sidewalls has emerged as a straightforward strategy.[48−51] Using this technique toward efficient electrochemical CO_2 reduction, recent examples have described the immobilization

Received: June 16, 2017
Published: September 8, 2017

DOI: 10.1021/jacs.7b06269
J. Am. Chem. Soc. 2017, 139, 14425−14435

Scheme 1. Schematic Representation of [MnBr(bpy$_{pyr}$)(CO)$_3$] (Mn$_{pyr}$) Immobilized on a CNT Sidewall, Concentration-Dependent Dimerization or Mn−H Formation, and Intermediate-Dependent Reduction of CO_2 to CO or HCOOH

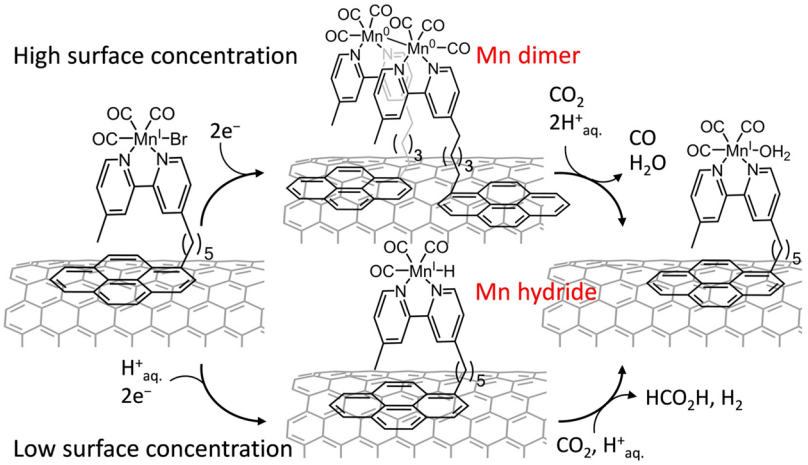

of Re,[52] Ir,[53] and Fe[54] based catalysts onto CNT matrixes, the latter two examples affording catalytic activity in aqueous solution.

The complex [MnBr(bpy)(CO)$_3$] (bpy = 2,2′-bipyridine) has become a noble metal-free model catalyst for CO_2 reduction thanks to the versatile and simple structure of the bpy ligand.[30] This catalyst exhibits high activity (turnover frequency up to 480 s^{-1}) in MeCN, and its catalytic mechanism has been studied in depth by changing the nature of the substituents on the bpy ligand.[12,13,55−61] The Mn catalyst was previously integrated onto CNTs using Nafion,[39,62] onto p-Si via polymerization,[63] and onto TiO_2 through a phosphonate anchoring group.[33] The latter system exhibited a record turnover number (TON) for the Mn catalyst of 112 in MeCN.[33] UV−vis spectroelectrochemistry (SEC) revealed that the grafted Mn catalyst dimerized on the electrode surface,[33] which has also been described in solution upon electrochemical reduction for this class of catalyst.[12] Although these studies showed enhancement of the catalytic properties of the Mn complex upon immobilization, the reported activity is still limited to organic solvents and low TONs (maximum of 101) in aqueous conditions.[39,62]

In this work, a novel *fac*-[MnBr(bpy)(CO)$_3$]-type complex bearing a pyrene anchoring unit was synthesized (**Mn$_{pyr}$**, Schemes 1 and 2). The pyrene unit allowed stable immobilization onto CNTs. The electrocatalytic activity of the compound was first studied toward the reduction of CO_2 in homogeneous organic solution (MeCN + 5% H_2O) and then in fully aqueous solutions after heterogenization on the CNT surface. The Mn catalyst modified electrodes were investigated using cyclic voltammetry (CV) and controlled-potential electrolysis (CPE). The surface loading of the Mn complex was found to have a distinct effect on the selectivity toward CO or $HCOO^-$ production (Scheme 1). Using transmission UV−vis and surface-sensitive IR SEC in the attenuated total reflection (ATR) mode, the different catalytic intermediates involved were investigated in situ. Upon decreasing the surface loading, the previously described dimer formation was lowered. Instead, formation of a putative hydride species was detected. The formation of one or the other catalytic intermediate is assigned to be decisive for selectivity toward either CO or $HCOO^-$ at different surface loadings.[55,61,64]

Scheme 2. (a) Synthetic Route to *fac*-[MnBr(bpy$_{pyr}$)(CO)$_3$] (Mn$_{pyr}$)[a]

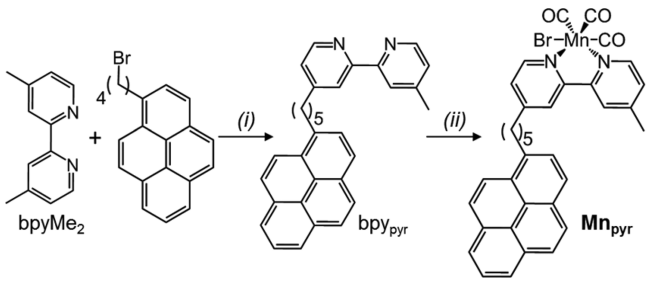

[a]Conditions: (i) Lithium diisopropylamide (LDA, 2 equiv), THF, 4 h, −10 °C, N_2 (77% yield); (ii) [MnBr(CO)$_5$] (1.25 equiv), Et_2O, 4 h, reflux, N_2 (83% yield).

RESULTS AND DISCUSSION

Synthesis and Characterization of Mn$_{pyr}$. 4-Methyl-4′-(5-(pyren-1-yl)pentyl)-2,2′-bipyridine (bpy$_{pyr}$) was synthesized by reacting a lithiated 4,4′-dimethyl-bipyridine intermediate with 1-(4-bromobutyl)pyrene, as previously described (Scheme 2).[65] The ligand bpy$_{pyr}$ was then refluxed with [MnBr(CO)$_5$] in dry Et_2O for 4 h to yield *fac*-[MnBr(bpy$_{pyr}$)(CO)$_3$] (**Mn$_{pyr}$**) with an overall yield of 64% (Scheme 2). The composition and purity of **Mn$_{pyr}$** were confirmed by ^{1}H, ^{13}C NMR, and FT-IR spectroscopy as well as mass spectrometry and elemental analysis (see the Experimental Section for details).

The electrochemical properties of **Mn$_{pyr}$** were investigated by CV in MeCN containing $TBAPF_6$ (0.1 M, TBA = tetrabutylammonium) at a glassy carbon working electrode (Figure 1a,b). In dry MeCN and under a N_2 atmosphere, the Mn^I complex exhibits two successive irreversible reduction processes at $^{red}E_p$ = −1.68 and −1.86 V vs Fc^+/Fc (see below for assignment of the reversible redox process at −2.48 V). According to literature assignments,[30] the first cathodic wave ($^{red,1}E_p$) is attributed to the reduction to Mn^0, followed by dimerization and formation of a Mn^0−Mn^0 species. The second cathodic process ($^{red,2}E_p$) is assigned to the one-electron reduction of the dimer to a mononuclear anionic species (Figure 1a).[30] The redox wave ($^{red,3}E_{1/2}$) observed at −2.48 V vs Fc^+/Fc is attributed to the reversible redox response of the bpy ligand.[30] Two anodic waves were observed following scan

DOI: 10.1021/jacs.7b06269
J. Am. Chem. Soc. 2017, 139, 14425−14435

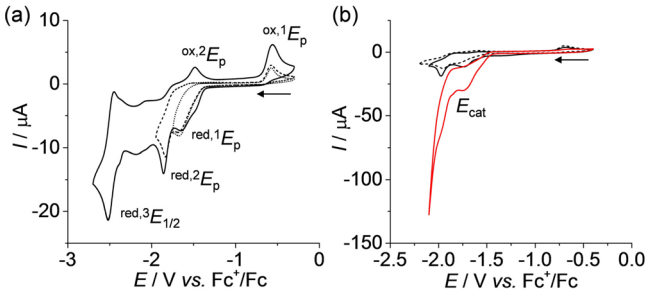

Figure 1. CV scans of $\mathbf{Mn}_{pyr}$ (1 mM) (a) in MeCN reversing the sweep at different potentials under N_2, (b) in MeCN under N_2 (black solid trace), in MeCN containing 5% H_2O under N_2 (black dashed trace), and in MeCN containing 5% H_2O under CO_2 (red trace). All CV scans were recorded with $TBAPF_6$ (0.1 M) as supporting electrolyte at a scan rate (ν) of 100 mV s^{-1} and room temperature with the scan start being indicated by an arrow.

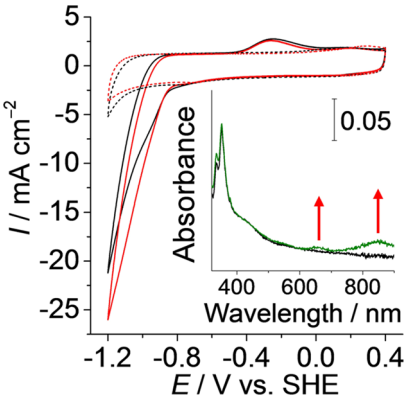

Figure 2. CV scans of the bare (unmodified) MWCNT electrodes (dashed traces) and CNT|$\mathbf{Mn}_{pyr}$ (solid traces) under N_2 (pH 8.2) (black traces) and CO_2 (pH 7.4) (red traces) in aqueous $KHCO_3$ (0.5 M) electrolyte solution at ν = 100 mV s^{-1} and room temperature. Inset: UV–vis spectra of the CNT|$\mathbf{Mn}_{pyr}$ electrode without applied bias (black trace) and at E_{app} = −1.1 V vs SHE (green trace) under CO_2.

reversal after $^{red,3}E_p$ at −1.49 and −0.57 V vs Fc^+/Fc, assigned to one-electron processes corresponding to the reoxidation of the mononuclear anionic ($^{ox,2}E_p$) and dimeric ($^{ox,1}E_p$) species, respectively.[30,56] The latter assignment was confirmed by scan reversal after $^{red,1}E_p$ and the observation of only the reoxidation of the dimer species at $^{ox,1}E_p$ = −0.57 V vs Fc^+/Fc.

Addition of 5% H_2O to the MeCN electrolyte solution does not show any significant increase in cathodic current, suggesting the limited ability of $\mathbf{Mn}_{pyr}$ to reduce protons under these conditions (Figure 1b). In contrast, purging this aqueous MeCN solution with CO_2 gas results in a large catalytic wave for CO_2 reduction with a catalytic onset potential (E_{cat}) of −1.51 V vs Fc^+/Fc, consistent with previous reports for the parent *fac*-[MnBr(bpy)$(CO)_3$] under the same conditions.[30]

Immobilization and Performance of $\mathbf{Mn}_{pyr}$. Immobilization of $\mathbf{Mn}_{pyr}$ onto a multiwalled carbon nanotube (MWCNT) electrode enabled the study of its electrocatalytic activity in fully aqueous solution. The Mn complex was anchored onto MWCNTs following an established two-step procedure:[51,66] First, a dispersion of MWCNTs in *N*-methylpyrrolidone (20 μL, 5 mg_{CNT} mL^{-1}) was drop-cast and dried on a glassy carbon disk electrode (diameter ø = 5 mm), giving a MWCNT electrode with 5 μm thickness. The catalyst was subsequently immobilized by immersing the MWCNT electrode into an anhydrous DMF solution of $\mathbf{Mn}_{pyr}$ (10 mM) for 30 min in the dark and at room temperature. The resulting CNT|$\mathbf{Mn}_{pyr}$ electrode was subsequently rinsed successively with DMF and water before CV experiments were undertaken (see below for more characterization details of the Mn-loaded MWCNT electrode).

CV scans recorded with CNT|$\mathbf{Mn}_{pyr}$ in aqueous $KHCO_3$ (0.5 M, pH 8.2) electrolyte solution under N_2 show an irreversible cathodic wave at $^{red}E_p$ = −1.0 V vs SHE ("shoulder" of solid black trace in Figure 2), which was assigned to the one-electron reduction of Mn^I to Mn^0. This Mn reduction wave overlaps with a dominant cathodic current that is mainly attributed to proton reduction (Figure 2, see below for more details). Following scan reversal, an irreversible anodic process, assigned to the reoxidation of the Mn^0 species,[39] can be observed at $^{ox}E_p$ = −0.24 V vs SHE. In the presence of CO_2 (pH 7.4), the current observed at $^{red}E_p$ is enhanced by a catalytic wave from reduction of CO_2. The observed onset potential (E_{cat} = −0.91 V vs SHE) with the immobilized $\mathbf{Mn}_{pyr}$ complex corresponds to a small overpotential (η = 360 mV for CO and/or η = 390 mV for formate production).[67] It is noteworthy that the irreversible anodic process at $^{ox}E_p$ is still present in the presence of CO_2 but displays a decrease in peak current. This observation may highlight that some of the immobilized and electrochemically reduced $\mathbf{Mn}_{pyr}$ does not readily react with CO_2 and is reoxidized at the electrode surface instead, which could possibly be due to limited diffusion of CO_2 within the CNT film. The bare ($\mathbf{Mn}_{pyr}$-free) MWCNT electrode does not show notable cathodic current enhancement in the presence of CO_2, confirming that the current enhancement observed with the CNT|$\mathbf{Mn}_{pyr}$ electrode solely arises from the presence of the catalyst on the electrode surface.

To confirm the formation of the dimeric Mn^0 species on the electrode surface upon reduction at $^{red}E_p$, transmission UV–vis SEC was carried out using $\mathbf{Mn}_{pyr}$ deposited onto MWCNT films on a transparent FTO glass substrate (see the Experimental Section for details). CV of CNT|$\mathbf{Mn}_{pyr}$ on FTO-coated glass was carried out to confirm the immobilization of the complex (Figure S1), and UV–vis absorption spectra of the electrodes without and with applied potential (E_{appl} = −1.1 V vs SHE) were compared in aqueous electrolyte solution (Figure 2, inset). Two bands appear at 655 and 850 nm under negative applied bias, which are comparable to the bands described previously for the dimer in solution and on a TiO_2 electrode in MeCN.[30,33] The UV–vis SEC analysis therefore supports generation of the Mn^0–Mn^0 dimer at the surface of the MWCNT electrode upon reduction at $^{red}E_p$.

To gain more insight into the overall activity, selectivity, and stability of the CNT|$\mathbf{Mn}_{pyr}$ electrode, CPE was performed at E_{appl} = −1.1 V vs SHE under CO_2 and the electroreduction products were analyzed using gas and ion chromatography (Figure 3). The CNT|$\mathbf{Mn}_{pyr}$ electrodes showed high current densities between −5 and −1.5 mA cm^{-2} during the first hour of CPE before stabilizing at approximately −0.5 mA cm^{-2} after 8 h (Figure S2), which coincides with a decrease in CO production activity (Figure 3a). Indeed, the electrodes showed good activity for CO production during the first hour, before stabilizing at 46 ± 11 μmol cm^{-2} CO. This decrease in CO production can be attributed to deactivation of the immobilized catalyst as it is commonly observed for molecular catalysts.[68] On the other hand, H_2 evolution remained stable over time and

DOI: 10.1021/jacs.7b06269
J. Am. Chem. Soc. 2017, 139, 14425–14435

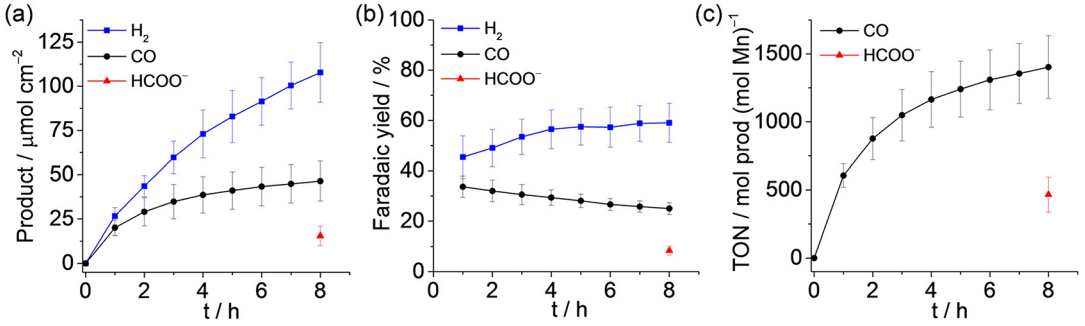

Figure 3. (a) Quantification and (b) cumulative Faradaic yields of H_2 (blue squares), CO (black circles), and formate (red triangle) production and (c) their corresponding TONs for CO and formate production as a function of CPE time at E_{appl} = −1.1 V vs SHE under CO_2 in aqueous $KHCO_3$ (0.5 M, pH 7.4) at room temperature.

reached a value of 108 ± 17 μmol cm^{-2} after 8 h. Some $HCOO^-$ was also detected at the end of CPE measurements (16 ± 5 μmol cm^{-2}).

Control CPE measurements on a bare (Mn-free) MWCNT electrode under CO_2 showed only small current densities of −0.3 mA cm^{-2}, with linear production of H_2 (26 μmol cm^{-2} after 8 h) and only traces of CO (Figure S3a). In addition, no CO was observed for a CNT|**Mn$_{pyr}$** electrode under N_2, whereas H_2 production was higher than that with the bare MWCNT electrode (47.2 μmol cm^{-2} after 8 h; Figure S3b). This observation confirms that the CO production solely arises from **Mn$_{pyr}$** on the electrode and in the presence of dissolved CO_2 in the electrolyte solution, whereas some H_2 is produced by the MWCNT scaffold under reductive conditions as well as by **Mn$_{pyr}$**. The high current densities and CO evolution rates during the first hours of CPE translated into a reasonable Faradaic yield for CO (Figure 3c), with a maximum yield of (34 ± 4)% being obtained after 1 h of CPE, before decaying to (25 ± 2)% cumulated after 8 h. In contrast, the efficiency for H_2 slightly increases over time and Faradaic yields of (45 ± 8) and (59 ± 8)% were observed after 1 and 8 h, respectively. For formate, a Faradaic yield of (8 ± 2)% was determined after 8 h, which results in a close-to-quantitative overall yield of (93 ± 4)% for all detected products.

The carbon source for the generated CO and $HCOO^-$ was confirmed by gas-phase IR spectroscopy and ^{1}H NMR spectroscopy, respectively. CPE under $^{13}CO_2$ resulted exclusively in ^{13}CO and $H^{13}COO^-$ (Figure S4). A TON_{Mn} of 1400 ± 230 was obtained for CO (Figure 3d), which is more than 10 times higher than previous results obtained electrochemically[30] or photochemically[59] using Mn(bpy)-type catalysts in organic[33] or aqueous[39,62] solution. Thus, the CNT|**Mn$_{pyr}$** electrode displays high activity for catalytic CO_2 to CO reduction in aqueous solution and compares well with noble metal-free solid-state electrocatalysts in terms of the TON at a low overpotential.[37,38,54,69,70] A respectable TON_{Mn} of 460 ± 120 was obtained for $HCOO^-$ production.

In order to verify the importance of immobilization and the molecular nature of the catalytically active species, a series of control experiments were carried out using anchor-free *fac*-[$MnBr(bpyMe_2)(CO)_3$] ($bpyMe_2$ = 4,4′-dimethyl-2,2′-bipyridine),[30] the precursors of **Mn$_{pyr}$** and Mn salts drop-cast (10 mM in DMF) onto the MWCNT electrode or in solution (Figure S5). CV of *fac*-[$MnBr(bpyMe_2)(CO)_3$] on the electrode shows the appearance of a catalytic feature when CO_2 is added to the fully aqueous electrolyte solution (Figure S5a). CPE performed on CNT|*fac*-[$MnBr(bpyMe_2)(CO)_3$] resulted in CO production with a TON_{Mn} of 237 after 8 h, which is approximately 6 times less than that obtained by using **Mn$_{pyr}$**. CV scans performed on the MWCNT electrode modified with [$MnBr(CO)_5$] or bpy_{pyr} with $MnCl_2$ (1 mM) in solution did not display a distinguishable catalytic wave under CO_2 (Figure S5b,c), and only traces of CO could be detected after 8 h of CPE (1.1 and 2.4 μmol cm^{-2} for [$MnBr(CO)_5$] and $bpy_{pyr}/MnCl_2$, respectively; Figure S5d). These results support that the high activity observed for CNT|**Mn$_{pyr}$** is not caused by possible degradation products of the molecular Mn catalyst. In addition, CV scans performed on CNT|**Mn$_{pyr}$** after CPE showed the appearance (although at reduced intensity) of identical redox behavior compared to pre-electrolysis measurements (Figure S6). The presence of the irreversible peak at $^{ox}E_p$ at −0.24 V vs SHE (due to dimer reoxidation in aqueous conditions[39]) and the catalytic wave at E_{cat} = −0.91 V vs SHE confirm that at least some of the molecular species remains on the surface throughout the CPE experiment without clearly observable degradation.

Tuning of Selectivity by Varying the Surface Loading. To study the dimerization of the heterogenized **Mn$_{pyr}$** catalyst in more detail, the influence of catalyst surface loading was investigated by incubating the MWCNT electrodes in solutions containing different concentrations of **Mn$_{pyr}$**. The electrochemical behavior of the electrodes with different surface loadings of **Mn$_{pyr}$** was subsequently examined. From integration of the oxidation wave in CV, the amount of electroactive **Mn$_{pyr}$** immobilized on the electrode can be estimated. The surface loading and the position of the oxidation peak of **Mn$_{pyr}$** immobilized onto MWCNTs was shown to be dependent on the **Mn$_{pyr}$** incubation concentration (Figure 4).

At higher surface loading, above 30 nmol cm^{-2} from incubation with 10 and 20 mM **Mn$_{pyr}$**, the dimer reoxidation peak was detected at $^{ox}E_p$ = −0.24 V vs SHE, close to the previously reported value.[39] At lower loading, below 20 nmol cm^{-2} from incubation with 0.5 and 1 mM **Mn$_{pyr}$**, a small irreversible reduction wave was observed at $^{red}E_p$ = −1.0 V vs SHE and the corresponding reoxidation wave was shifted considerably to $^{ox}E_p$ = −0.34 V vs SHE (100 mV more cathodic than the response at higher surface loadings). At intermediate surface loadings, between 20 and 30 nmol cm^{-2} from incubation with 2.5 and 5 mM **Mn$_{pyr}$**, a broadened oxidation wave was attributed to a convoluted response from both anodic processes. For all **Mn$_{pyr}$** surface loadings, a strong reduction wave followed the reduction of the Mn^I to Mn^0 ($^{red}E_p$ = −1.0 V vs SHE), which is assigned to the reduction of protons to H_2 under a N_2 atmosphere (see above). This catalytic reduction

DOI: 10.1021/jacs.7b06269
J. Am. Chem. Soc. 2017, 139, 14425−14435

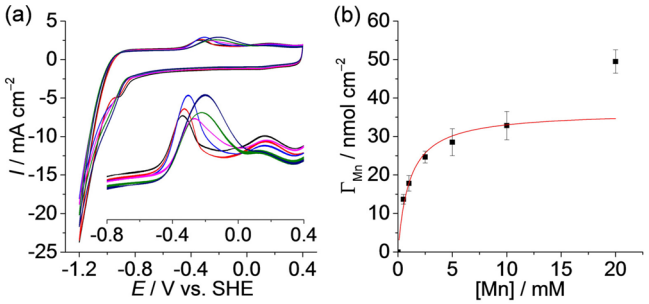

Figure 4. (a) CV scans of CNT|$\mathbf{Mn_{pyr}}$ loaded from incubation of the MWCNT electrode in $\mathbf{Mn_{pyr}}$ solutions at different concentrations: 0.5 (black); 1 (red); 2.5 (blue); 5 (purple); 10 (green); and 20 mM (navy) in aqueous $KHCO_3$ (0.5 M) electrolyte solution under N_2 at pH 8.2 (ν = 100 mV s^{-1}) at room temperature. (b) Variation of $\mathbf{Mn_{pyr}}$ surface loadings depending on incubation of the MWCNT electrode in different $\mathbf{Mn_{pyr}}$ concentrations (0.5, 1, 2.5, 5, 10, and 20 mM), experimental data (black squares), and fitted adsorption isotherm (red trace).

wave becomes more dominant at lower surface loadings of $\mathbf{Mn_{pyr}}$ (Γ_{Mn}).

Γ_{Mn} increased with the concentration of the incubation solution until reaching a plateau between 5 and 10 mM, following a Langmuir isotherm (see the Experimental Section and Figure 4b).[66,71] The best fit (using Mn concentrations, [Mn], up to 10 mM) was obtained with a saturation surface concentration, $\Gamma_{Mn,max}$, of 36.5 nmol cm^{-2} and with a K_{Mn} of 950 L mol^{-1}, in line with previously reported values for pyrene-bearing coordination complexes.[66] The surface loading after incubation with the highest $\mathbf{Mn_{pyr}}$ concentration (20 mM) does not align with the fit, which can be rationalized by oversaturation of the surface at higher incubation concentrations. At $\Gamma_{Mn,max}$, the probability for $\mathbf{Mn_{pyr}}$ to dimerize on the surface during electroreduction is high. On the other hand, for lower Γ_{Mn}, the probability of two $\mathbf{Mn_{pyr}}$ units being close enough to each other to form a dimer is substantially decreased. The altered surface loading therefore gives a possible explanation for the different electrochemical response of $\mathbf{Mn_{pyr}}$. At lower surface concentration, impeded dimerization would lead to the formation of another reduced species and the oxidation peak observed at $^{ox}E_p$ = −0.33 V vs SHE could possibly be attributed to the one-electron oxidation of a single Mn^0 complex back to the Mn^I complex.

As the CV response of $\mathbf{Mn_{pyr}}$ changed as a function of catalyst loading, the possible impact of Γ_{Mn} on the catalytic activity and selectivity was studied by CPE coupled to H_2, CO, and formate analysis. Figure 5 summarizes the results and shows clear trends (see Figures S7 and S8 for the complete data set). Lowering the surface loading of $\mathbf{Mn_{pyr}}$ on MWCNTs resulted in a decrease in overall CO production from 62 ± 15 μmol cm^{-2} at high Γ_{Mn} (50 ± 3 nmol cm^{-2}) to 26 ± 5 μmol cm^{-2} at low Γ_{Mn} (14 ± 1 nmol cm^{-2}), which is consistent with less Mn dimer available for CO_2 reduction (Figure 5c). The TON_{Mn} for CO remained between 1500 and 2000 independent of the surface loading. However, the production of $HCOO^-$ increased substantially, from 19 ± 1 μmol cm^{-2} at high Γ_{Mn} (50 ± 3 nmol cm^{-2}) to 54 ± 7 μmol cm^{-2} at low Γ_{Mn} (14 ± 1 nmol cm^{-2}), thus leading to a high TON_{Mn} for $HCOO^-$ generation of 3920 ± 230 (Figure S9). This increase of $HCOO^-$ production appears to be inversely correlated to the surface loading of the catalyst and starts to become predominant when Γ_{Mn} reaches values lower than 25 nmol cm^{-2} (Figures 4b and S8), which is significantly lower than $\Gamma_{Mn,max}$ estimated from the Langmuir isotherm. In addition to the increased production of $HCOO^-$, the production of H_2 is also greatly enhanced at lower catalyst loading, from 90 ± 4 μmol cm^{-2} at high Γ_{Mn} (50 ± 3 nmol cm^{-2}) to 225 ± 27 μmol cm^{-2} at low Γ_{Mn} (14 ± 1 nmol cm^{-2}).

Several *fac*-[MnBr(bpy)$(CO)_3$] systems have already been described for the photocatalytic[57,59,64] or electrocatalytic[55,61] reduction of CO_2 to $HCOO^-$, and for this transformation, a Mn-hydride is thought to be the active catalytic intermediate. This Mn−H intermediate was recently characterized using IR-SEC in solution, and it was shown that the $HCOO^-$ production is greatly enhanced by the addition of strong Brønsted acids through more favorable formation of the transient Mn−H species.[61] In agreement, at low surface loadings of $\mathbf{Mn_{pyr}}$, dimerization is less likely, giving rise to a monomeric reduced Mn^0 species that is suggested to form a transient Mn−H upon further reduction in aqueous solution (below the $^{red}E_p$ of −1.0 V vs SHE). The Mn−H can then preferentially produce H_2 and $HCOO^-$ over CO (Scheme 1).

Spectroelectrochemistry of $\mathbf{Mn_{pyr}}$ Dimerization. IR SEC was employed to obtain structural information on the catalytically relevant states of the immobilized $\mathbf{Mn_{pyr}}$ at different surface loadings. Specifically, the CO stretching vibrations, ν(CO), were monitored as their frequencies strongly depend on the electronic properties (i.e., oxidation state and coordination environment) of the metal atom.[72,73] Although ATR IR SEC has previously been used for the in situ study of active sites of adsorbed enzymes (on graphite nanoparticles[74] and Au-modified surfaces[75,76]) as well as for probing bulk catalytic reactions,[77,78] only a few examples applied this method

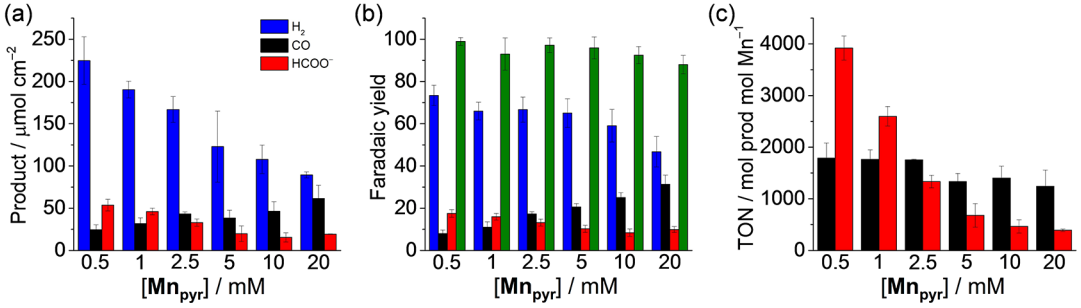

Figure 5. Product analysis following 8 h of CPE at E_{appl} = −1.1 V vs SHE in aqueous $KHCO_3$ (0.5 M, pH 7.4) under CO_2 at room temperature: (a) Total amounts, (b) Faradaic yields, and (c) TON_{Mn} for CNT|$\mathbf{Mn_{pyr}}$ electrodes prepared from different $\mathbf{Mn_{pyr}}$ incubation concentrations. Color-coding: H_2 (blue), CO (black), $HCOO^-$ (red), and total (green).

DOI: 10.1021/jacs.7b06269
J. Am. Chem. Soc. 2017, 139, 14425−14435

to investigate heterogenized synthetic molecular catalysts.[79,80] An IR signal enhancing Au layer is usually required to obtain the necessary signal intensity to analyze a surface-attached cocatalyst. To tackle the limitations of established approaches, we employed a modified ATR IR SEC setup to allow an in-depth study of the immobilized molecular Mn catalyst on the MWCNT-coated Si prism as the working electrode under in situ conditions (Figure S10).

Incubation of the MWCNT electrode with $\mathbf{Mn}_{\mathbf{pyr}}$ (10 mM in dry DMF) afforded intense IR signals of the catalyst. In particular, well-resolved ν(CO) bands in the region from 1800 to 2050 cm^{-1} were observed (Figure 6a). As the evanescent IR wave exhibits a penetration depth of about 0.5 μm in this experimental configuration,[81] this spectral feature should exclusively result from immobilized $\mathbf{Mn}_{\mathbf{pyr}}$ molecules with ν(CO) frequencies at 2022, 1930, and 1912 cm^{-1} for the facially coordinated tricarbonyl metal complex.[73] These frequencies match well those of unmodified [MnBr(bpy)-$(CO)_3$] in MeCN solution,[73] indicating once again that introduction of the pyrene linker does not significantly influence the electronic properties of the Mn center (Table 1). The observation of intense and distinctly resolved ν(CO) bands demonstrates that ATR IR is sufficiently sensitive to probe $\mathbf{Mn}_{\mathbf{pyr}}$ on the MWCNT electrode in this experimental configuration.

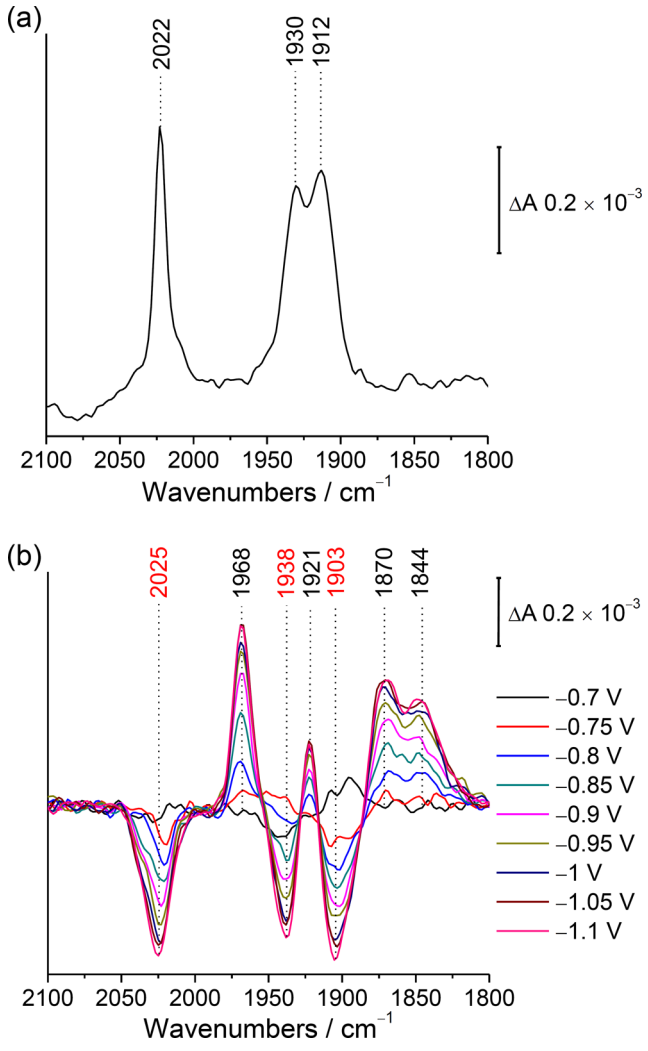

Figure 6. ATR IR spectra of a CNT|$\mathbf{Mn}_{\mathbf{pyr}}$ electrode. (a) Absorbance spectra showing the ν(CO) bands of $\mathbf{Mn}_{\mathbf{pyr}}$ on a MWCNT electrode in DMF (incubated from a 10 mM solution of $\mathbf{Mn}_{\mathbf{pyr}}$). The ν(CO) modes are observed at 2022, 1930, and 1912 cm^{-1}. (b) Potential-dependent (vs SHE) difference spectra of $\mathbf{Mn}_{\mathbf{pyr}}$ in aqueous $KHCO_3$ (0.5 M) under argon and at room temperature with the reference spectrum recorded at 0 V (fully oxidized conditions) prior to each measurement. Reduction causes an increase of ν(CO) located at 1968, 1921, 1870, and 1844 cm^{-1} (black numbers) and the disappearance of the bands at 2025, 1938, and 1903 cm^{-1} (red numbers).

Negative potentials were applied in aqueous $KHCO_3$ solution (0.5 M, pH 8.2) to monitor the reduction of the immobilized $\mathbf{Mn}_{\mathbf{pyr}}$ catalyst through the surface-sensitive ATR IR SEC approach. Figure 6b displays IR difference spectra at increasingly negative electrode potentials (a spectrum at 0 V vs SHE was used prior to each potential step as a reference spectrum). Major spectral differences were only observed at potentials more negative than −0.7 V vs SHE, upon which the appearance of bands located at 1968, 1921, 1870, and 1844 cm^{-1} was accompanied by a decrease of bands at 2025, 1938, and 1903 cm^{-1} (Table 1). Note that the absolute frequencies of the latter two bands are difficult to determine as the band at 1921 cm^{-1} increases upon reduction. Accordingly, the stated frequencies are estimated. Plotting the intensity of the positive bands at 1968 and 1870 cm^{-1} as the function of poised electrode potential yielded sigmoidal curves that could be fitted with the Nernst equation affording matching midpoint potentials at −0.84 ± 0.05 V vs SHE for both redox transitions (see the Experimental Section and Figure S11). The concomitant rise and the matching midpoint potentials indicate that these bands belong to the same redox species.

The band at 1921 cm^{-1} was not considered because two neighboring negative bands at 1938 and 1902 cm^{-1} masked its intensity (see above). The appearance of the four ν(CO) bands upon applying reductive conditions is indicative of the formation of a Mn^0 dimer species, as previously reported.[56,73] A fifth band (predicted at around 1963 cm^{-1} from previous measurements in THF[73]) is known to exhibit only weak IR absorption; therefore, it is most likely masked by the more intense adjacent 1968 cm^{-1} absorption.[56,73] A frequency downshift (up to −15 cm^{-1} compared to literature values in organic solvents listed in Table 1) is observed in this work, which may be attributed to decreased electron density at the CO bond resulting from hydrogen bonding to the carbonyl oxygen atoms in aqueous electrolyte solution.[82] The assignment of these bands to a Mn^0 dimer is also supported by the UV−vis SEC experiments above (Figure 2, inset). No indication for the presence of another reduced species was found by IR SEC under the applied conditions.

Reoxidation of the dimer was monitored with IR SEC by a stepwise increase of the potential from −0.8 to 0 V (fully oxidized state) vs SHE. Figure 7a shows the resulting difference spectra (a reference spectrum was recorded under fully reduced conditions, E_{appl} = −1.1 V vs SHE, prior to each potential step). The previously observed set of bands located at 2025, 1938, and 1903 cm^{-1} re-emerges upon applying E_{appl} > −0.5 V vs SHE at the expense of bands assigned to the dimer species (see above). Upon comparison with literature reports, the emerging ν(CO) bands are assigned to formation of a (monomolecular) Mn^I complex upon reoxidation of the dimer. As the initial generation of the dimer complex involves removal of the bromide ligand, the state formed at more positive potentials most likely represents a Mn^I complex with the bromido ligand being replaced by the solvent water (Table 1).[13,73] Thus, the

DOI: 10.1021/jacs.7b06269
J. Am. Chem. Soc. 2017, 139, 14425−14435

Table 1. Frequencies of ν(CO) for Mn_{pyr} Adsorbed on MWCNT Electrodes under Different Conditions and Respective Assignment to Different Mn_{pyr} Species Based on Comparison to Literature Values Obtained in Solution[a]

this work		comparison to literature	
ν(CO)/cm^{-1}	assignment	ν(CO)/cm^{-1}	assignment
2022, 1930, 1912	$[Mn^{I}Br(bpy_{pyr})(CO)_3]$	2023, 1935, 1914 (THF)[73]	$[Mn^{I}Br(bpy)(CO)_3]$
2025, 1938*, 1903*	$[Mn^{I}(H_2O)(bpy_{pyr})(CO)_3]^+$	2019, 1933, 1919 (MeCN)[73]	$[Mn^{I}(solvent)(bpy)(CO)_3]^+$
1968, 1921, 1870, 1844	$[Mn^{0}(bpy_{pyr})(CO)_3]_2$	1973, 1928, 1878, 1858 (MeCN)[56] 1975, 1963 (weak), 1936, 1886, 1866 (THF)[73]	$[Mn^{0}(bpy)(CO)_3]_2$
not detected	$[Mn(bpy_{pyr})(CO)_3]^-$	1909, 1811 (THF)[73]	$[Mn(bpy)(CO)_3]^-$
1991, 1880	$[Mn^{I}(H)(bpy_{pyr})(CO)_3]$	1991, 1888 (MeCN)[61]	$[Mn^{I}(H)(bpy)(CO)_3]$

[a]The asterisk assigns estimated frequencies.

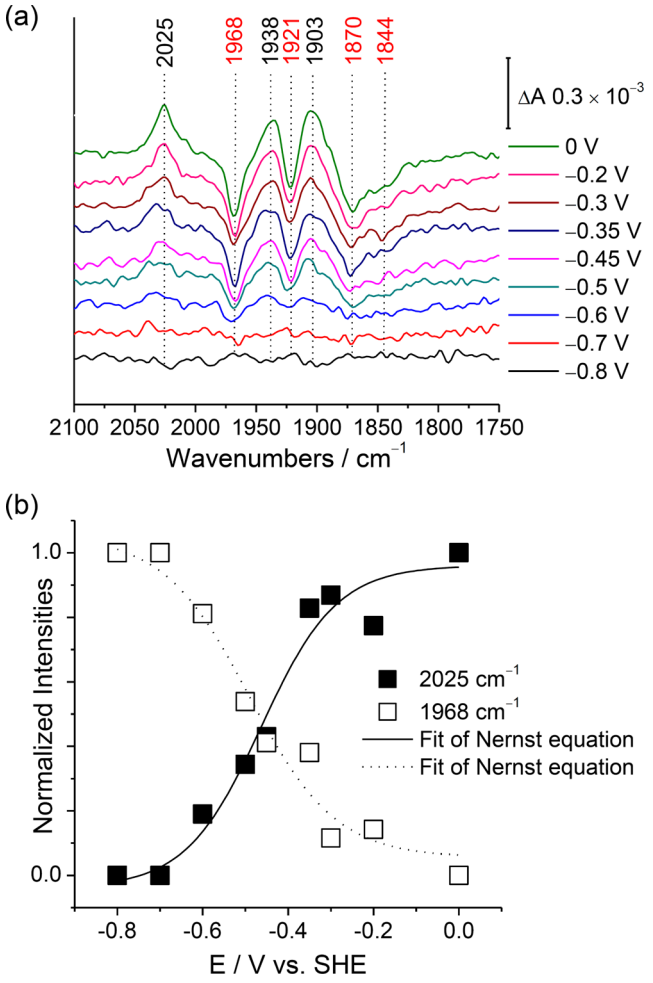

Figure 7. Reoxidation of the Mn^0 dimer species at positive potentials in aqueous $KHCO_3$ solution (0.5 M, pH 8.2) under Ar at room temperature. (a) ATR IR difference spectra of the reoxidation of $\mathbf{Mn_{pyr}}$ at different potentials (vs SHE; reference spectrum recorded at E_{appl} = −1.0 V). ν(CO) bands located at 2025, 1983, and 1903 cm^{-1} (black numbers) increase at the expense of the prior observed marker bands (for the dimer state) at 1968, 1921, 1870, and 1844 cm^{-1} (red numbers). (b) Intensity of the bands at 2025 (black squares) and 1968 cm^{-1} (hollow squares) as a function of electrode potential. Lines correspond to a fit of the Nernst equation to the data set.

observed ν(CO) frequencies are slightly shifted compared to those found for the bromide-bound $\mathbf{Mn_{pyr}}$ complex (Figure 6a, Table 1).[64] Figure 7b shows the normalized intensity of the bands at 2025 and 1968 cm^{-1}, representing the two different redox species (i.e., Mn^0−Mn^0 dimer vs monomolecular Mn^I species) as a function of electrode potential. Both intensities follow the same trend with opposite signs, and the data sets can be fitted satisfactorily using the Nernst equation with matching apparent midpoint potentials (Figure 7b). This observation points to a coupled redox events, in which dimer oxidation directly affords formation of the Mn^I species with marker bands identified at 2025, 1938, and 1903 cm^{-1}.

Spectroelectrochemistry at Low Mn_{pyr} Loading. The change in selectivity of product formation from high to low loading of adsorbed $\mathbf{Mn_{pyr}}$ and the suggested change in mechanism for CO_2 reduction were also probed by IR SEC. An obvious challenge in this SEC analysis was associated with the monitoring of very low concentrations of $\mathbf{Mn_{pyr}}$ and the resulting weak ν(CO) frequencies, which made a reliable evaluation difficult. We have therefore incubated from a relatively high concentration of $\mathbf{Mn_{pyr}}$ (10 mM in DMF) and followed the decreasing $\mathbf{Mn_{pyr}}$ surface loading over time by performing repetitive CV scans (scanning between −1.1 and 0 V vs SHE at ν = 50 mV s^{-1}) of the CNT|$\mathbf{Mn_{pyr}}$ electrode in aqueous $KHCO_3$ solution (0.5 M, pH 8.2). The progress of slow $\mathbf{Mn_{pyr}}$ loss from the MWCNT electrode can be analyzed by following the decreasing anodic wave ($^{ox}E_p$; see above), and the catalytic intermediates are monitored through IR SEC by tracking the intensity of the strongest dimer band at 1968 cm^{-1} formed upon reduction (E_{appl} = −1.0 V vs SHE, reference spectrum recorded at 0 V vs SHE). The electroactive $\mathbf{Mn_{pyr}}$ surface concentration was reduced by approximately 50% after 400 CV scans (Figure S12). The $\mathbf{Mn_{pyr}}$ film loss may be due to desorption or decomposition of the immobilized $\mathbf{Mn_{pyr}}$ complex. Only two reduced Mn species carrying CO ligands were observed, which can be consistently assigned to reduced species of the intact $\mathbf{Mn_{pyr}}$ catalyst on the surface (see below). Possible decomposition of the molecular $\mathbf{Mn_{pyr}}$ would not interfere with the IR SEC experiment as ν(CO) frequencies were selectively monitored.

Figure 8 shows the surface-sensitive IR difference spectra after incubation as a reference and after 200 and 400 CV scans. After incubation, reduction of $\mathbf{Mn_{pyr}}$ at E_{appl} = −1.0 V vs SHE afforded the spectral pattern as discussed above (Figure 6b), indicating the formation of the Mn^0−Mn^0 dimer species. Lowering of the concentration of $\mathbf{Mn_{pyr}}$ is consistent with a decrease in the overall signal intensity of the dimer bands (at 1968, 1870, and 1844 cm^{-1}) and the appearance of spectral features at 1991 and 1880 cm^{-1}. Stepwise reduction by applying potentials from −0.7 to −1.0 V vs SHE revealed that the new spectral features in the spectrum in Figure 8 were almost reversibly formed only upon reduction of the catalyst (Figure S13). Further decrease of Γ_{Mn} afforded the increase of the latter bands, which dominate the spectrum upon reduction.

To verify that these two bands belong to the same redox species, band analysis for the spectra recorded after 200 and

DOI: 10.1021/jacs.7b06269
J. Am. Chem. Soc. 2017, 139, 14425−14435

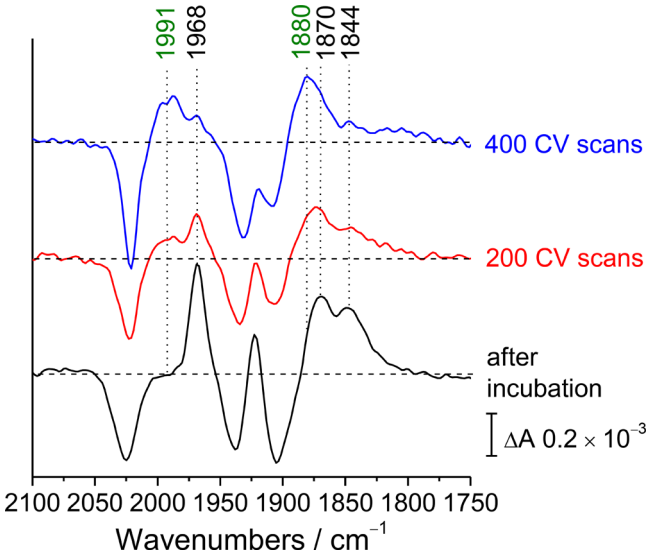

Figure 8. ATR IR difference spectra monitoring the reduced species of $\mathbf{Mn_{pyr}}$ at E_{appl} = −1.0 V vs SHE (reference spectrum recorded at 0 V vs SHE at fully oxidized conditions) as a function of decreasing surface concentration (0.5 M aqueous $KHCO_3$, pH 7.4). Successive lowering of the surface concentration was achieved by performing CV scans at a scan rate of 50 mV s^{-1}. The band intensity at 1968 cm^{-1} is used to monitor the overall decrease in concentration (black numbers indicate the Mn^0 dimer). At lowered surface concentrations, bands at 1991 and 1880 cm^{-1} (green numbers) arise that are assigned to ν(CO) stretching vibrations of a Mn-hydride species (Table 1).

400 CV scans was performed (Figure 8). Lorentzian band profiles were chosen for the positive bands, and their intensity and half-width iteratively varied until full reconstruction of the (positive parts of the) experimental spectra (Figure S14a). The bands at 1991 and 1880 cm^{-1} do not alter in relative intensity in the red and blue spectra in Figure 8, indicating that they belong to the same spectral component, that is, redox species. For comparison, such behavior is also observed for the bands at 1968 and 1844 cm^{-1} (Figure S14), which is expected as these bands are assigned to the dimer species, as demonstrated above (see Figure S11). The bands at 1991 and 1880 cm^{-1} likely represent a Mn-hydride complex that is formed upon reduction under these conditions, which is supported by the striking match between observed and literature-reported band frequencies for measured and calculated Mn-hydride complexes (Table 1).[61] Furthermore, the species is reversibly formed only upon reduction, and the presence of an anionic species (i.e., the $[Mn(bpy_{pyr})(CO)_3]^-$ species) can be ruled out as this species would be indicated by two strong ν(CO) bands located at approximately 1910 and 1811 cm^{-1}.[73] While the first band may be masked by the negative bands of the oxidized $\mathbf{Mn_{pyr}}$, no indication for the latter is observed in any of the recorded spectra upon reduction at potentials down to −1.1 V vs SHE. Finally, the assignment of a Mn-hydride species is also in accordance with preferential formation of formate and H_2 upon CPE experiments using lowered $\mathbf{Mn_{pyr}}$ surface concentrations, providing thereby an explanation for the switch in reactivity. Accordingly, the SEC IR experiments demonstrate that low concentrations of $\mathbf{Mn_{pyr}}$ favor formation of the hydride over the dimer species, and the long-term CPE measurements reflect the catalytic consequences of this change in mechanism.

The application of our surface-sensitive ATR IR SEC configuration allowed the effective in situ detection of catalytically relevant states of the immobilized $\mathbf{Mn_{pyr}}$ complex. Formation of the Mn^0–Mn^0 dimer species as well as the monomeric reduced Mn–H complex could be characterized on a MWCNT electrode surface. Notably, the presence of the two species could be directly linked to the electrocatalytic product selectivity (CO via the dimer and $HCOO^-$ and H_2 via the Mn-hydride).

CONCLUSIONS

This work describes the synthesis, electrochemistry and SEC characterization of a Mn CO_2 reduction catalyst immobilized through a pyrene anchoring group on a MWCNT electrode. Despite the low Faradaic yield for CO and formate, the hybrid electrode displays high activity for electrocatalytic reduction of aqueous CO_2 with TONs of up to 1790 ± 290 for CO and up to 3920 ± 230 for formate at E_{appl} = −1.1 V vs SHE (corresponding to overpotentials of η = 550 mV for CO and η = 590 mV for formate production). Product selectivity can be fine-tuned by controlling the surface loading of the catalyst on the CNT sidewalls. Low Mn catalyst loadings afford selectivity for the generation of dissolved formate, whereas high loading result in higher selectivity for gaseous CO. Control over product selectivity is a first step to rationally synthesize desired high-value products from CO_2 on demand.

In situ ATR IR and UV–vis SEC characterization of the molecular catalyst on the electrode surface allowed distinguishing between two different catalytic pathways by detecting the involved intermediates. The identified Mn dimer and Mn-hydride species formed on the electrode surface could be directly linked to the occurrence of distinct catalytic products. The implementation of such surface-sensitive in situ spectroscopy therefore proves to be of importance for understanding catalytic reactions of surface-bound molecular catalysts, stimulating future interdisciplinary research also beyond CO_2 reduction and MWCNT electrodes.

Overall, the present study highlights the benefits of rational incorporation of molecular catalysts onto electrode surfaces. Our strategy allowed enhancement of the catalytic activity and stability, as well as tuning of the selectivity of the immobilized catalyst, while enabling a detailed understanding of the catalytic mechanisms involved through the use of a powerful SEC approach.

EXPERIMENTAL SECTION

Materials and Reagents. Dry tetrahydrofuran (THF), diethyl ether (Et_2O), and acetonitrile (MeCN) were used for the synthesis and electrochemistry of the compounds. 4,4′-Dimethyl-2,2′-bipyridine ($bpyMe_2$), $[MnBr(CO)_5]$, *n*-BuLi (1.6 M in hexane), diisopropylamine, *N*-methyl-2-pyrrolidone, dimethylformamide (DMF), fluorine-doped tin oxide (FTO), tetrabutylammonium hexafluorophosphate ($TBAPF_6$), $KHCO_3$ (99.95% purity), and MWCNTs (thin and short, 755117 Aldrich, purity 95%) were purchased from Sigma-Aldrich. Column chromatography was carried out using silica gel 60 (0.040–0.063 mm mesh) from Merck. Other chemicals and solvents were purchased from commercial suppliers and used as received. 1-(4-Bromobutyl)pyrene[83] and the complex $[MnBr(bpyMe_2)(CO)_3]$[30] were synthesized and characterized as previously described. ^1H and ^{13}C NMR spectra were recorded on a Bruker DPX-400 MHz spectrometer at room temperature. High-resolution mass spectra were recorded using a ThermoScientific Orbitrap Classic mass spectrometer. The ATR FT-IR spectrum of $\mathbf{Mn_{pyr}}$ was recorded on a Nicolet iS50 spectrometer. Elemental analysis was carried out by the Microanalysis Service of the Department of Chemistry, University of Cambridge, using a PerkinElmer 240 Elemental Analyzer.

DOI: 10.1021/jacs.7b06269
J. Am. Chem. Soc. 2017, 139, 14425–14435

Synthesis of bpy_{pyr}. Diisopropyl amine (0.33 mL, 2.35 mmol) was added to THF (10 mL). The mixture was cooled to −10 °C with an ice/acetone bath. A solution of *n*-BuLi (1.6 M, 1.5 mL, 2.4 mmol) was slowly added to the reaction mixture and stirred for another 5 min at −10 °C under a N_2 atmosphere. Then, $bpyMe_2$ (230 mg, 1.25 mmol) in THF (40 mL) was added dropwise to the mixture (over 15 min) and further stirred for 10 min at −10 °C under a N_2 atmosphere. Then, 1-(4-bromobutyl)pyrene (400 mg, 1.2 mmol) in THF (40 mL) was added slowly to the mixture (over approximately 30 min), and stirred for another 30 min at −10 °C under N_2 atmosphere. Cold water (60 mL) was slowly added, followed by CH_2Cl_2 (80 mL). The product was extracted twice with CH_2Cl_2 (80 mL), dried over $MgSO_4$, and the solvent evaporated to dryness. The crude product was purified by column chromatography on silica gel using CH_2Cl_2/MeCN (9:1), yielding the product as an off-white solid. Yield: 410 mg, 77%. ^{1}H NMR ($CDCl_3$, 400 MHz): δ_H (ppm) = 1.50−1.60 (m, 2H), 1.80 (q, J = 7.8 Hz, 2H), 1.91 (q, J = 7.7 Hz, 2H), 2.44 (s, 3H), 2.72 (t, J = 7.8 Hz, 2H), 3.34 (t, J = 7.8 Hz, 2H), 7.08−7.15 (m, 2H), 7.84 (d, J = 7.7 Hz, 1H), 7.95−8 (m, 1H), 8−8.04 (m, 2H), 8.06−8.12 (m, 2H), 8.12−8.18 (m, 2H), 8.22−8.28 (m, 3H), 8.52 (d, J = 4.9 Hz, 2H). ^{13}C NMR ($CDCl_3$, 100 MHz): δ_C (ppm) = 21.3, 29.4, 30.4, 31.6, 33.5, 35.5, 121.5, 122.2, 123.4, 124.1, 124.7, 124.8, 124.9, 125.1, 125.2, 126.6, 127.2, 127.3, 128.6, 129.8, 130.9, 131.5, 136.9, 148.8. MS (+ESI, m/z): calcd. for $C_{32}H_{28}N_2$ $[M + H]^+$: 441.23 ; found, 441.25.

Synthesis of Mn_{pyr}. $[MnBr(CO)_5]$ (57 mg, 0.21 mmol) was added to Et_2O (15 mL) under a N_2 atmosphere. Then, bpy_{pyr} (75 mg, 0.17 mmol) was added, and the mixture was refluxed for 4 h in the dark. The mixture was then cooled to room temperature, and the orange precipitate was filtered off and washed with Et_2O (50 mL) and dried under high vacuum at room temperature to give the product as an orange solid. Yield: 93 mg, 83%. The light-sensitive compound was stored in the dark, and all electrochemical experiments were executed in the absence of light. ^{1}H NMR ($CDCl_3$, 400 MHz): δ_H (ppm) = 1.5−1.65 (br, 2H), 1.68−1.8 (m, 2H), 1.86−1.96 (m, 2H), 2.45−2.55 (m, 3H), 2.66−2.78 (2H), 3.30−3.40 (m, 2H), 7.20−7.30 (m, 2H), 7.75−7.95 (m, 3H), 7.95−8.05 (m, 3H), 8.05−8.20 (m, 4H), 8.20−8.30 (m, 1H), 8.95−9.10 (m, 2H). ^{13}C NMR ($CDCl_3$, 100 MHz): δ_C (ppm) = 21.3, 29.1, 30.1, 31.5, 33.3, 35.3, 122.1, 122.9, 123.3, 124.8, 125.0, 125.9, 126.4, 126.7, 127.3, 127.5, 128.6, 129.8, 130.8, 131.5, 150.2, 153.1, 154.6, 155.3, 221.8. FT-IR ATR (ν/cm^{-1}): 2016 (CO), 1900 (CO) (br). MS (+ESI, m/z): calcd. for $C_{35}H_{28}BrMnN_2O_3$ $[M - Br]^+$: 579.15; found, 579.19. Elemental analysis: calcd. for $C_{35}H_{28}BrMnN_2O_3$: C, 63.8; H, 4.3; N, 4.3; Br, 12.1; found: C, 64.2; H, 4.4; N, 3.9; Br, 12.1.

Electrodes for CV and CPE. MWCNT/glassy carbon electrodes were drop-cast by adding 20 μL of a 5 mg mL^{-1} dispersion of MWCNTs in *N*-methylpyrrolidone onto a glassy carbon electrode, and the deposit was dried under high vacuum before use. A 5 μm thick homogeneous MWCNT film was obtained as reported previously (0.2 cm^2 geometrical surface, ø = 5 mm).[66] The MWCNT/glassy carbon electrodes were soaked in a solution of $\mathbf{Mn_{pyr}}$ in dry DMF for 30 min in the dark. The modified electrode was subsequently rinsed with DMF and deionized water. Control experiments were performed with $[MnBr(bpyMe_2)(CO)_3]$, $MnCl_2$/bpy_{pyr}, and $[MnBr(CO)_5]$ instead of $\mathbf{Mn_{pyr}}$.

Electrodes for UV−Vis SEC. A MWCNT film was prepared as previously described.[84] Briefly, 2 mg of MWCNTs were sonicated in 500 mL of deionized water for 30 min and left to settle overnight. Then 200 mL of the supernatant were filtered over a cellulose nitrate filter (Millipore, 0.45 μm pore size, overall diameter of ø = 3.5 cm), leading to the homogeneous MWCNT film. The MWCNT film was subsequently deposited on a 2 × 1 cm glass slide with the top 1 × 1 cm coated with FTO (so that the MWCNT film covered both FTO-coated and bare glass areas) by carefully dissolving the cellulose filter with several washings of acetone, leading to the MWCNT film on FTO glass. The $\mathbf{Mn_{pyr}}$ modified electrode was obtained by drop-casting 10 μL of a 10 mM solution of $\mathbf{Mn_{pyr}}$ onto the MWCNT/FTO electrode (geometrical surface area of 0.25 cm^2) in the dark. After 10 min, the electrode was rinsed with deionized water and the FTO-coated portions of the electrode were not exposed to the electrolyte solution to prevent reductive degradation of FTO from influencing the spectra.

Electrodes for ATR IR SEC. The MWCNT films were deposited onto the Si substrate by carefully dissolving the cellulose filter with several washings of acetone, leading to the MWCNT film. The $\mathbf{Mn_{pyr}}$ modified electrode was obtained by drop-casting 10 μL of a 10 mM solution of $\mathbf{Mn_{pyr}}$ onto the CNT surface in the dark. After 10 min, the electrode was rinsed with DMF and with deionized water.

Electrochemistry. All electrochemical measurements were performed on a PalmSens EmStat or MultiEmStat^{3+} potentiostat in the dark. Electrochemistry in organic media was performed in MeCN containing 0.1 M $TBAPF_6$ in a three-electrode configuration using a Ag/AgCl wire as the reference electrode and a platinum mesh as the counter electrode. Ferrocene was used as the internal reference at the end of the measurements.

Aqueous electrochemistry was performed in $KHCO_3$ (99.95%, 0.5 M) electrolyte solution using a three-electrode configuration using a Ag/AgCl (sat. KCl) reference electrode and platinum mesh as the counter electrode. The potentials were converted from Ag/AgCl to standard hydrogen electrode (SHE) by adding +0.199 V. The CV and CPE measurements were carried out in a three-necked two-compartment cell separated by a Nafion membrane under N_2 or CO_2. The working electrode compartment was stirred during the CPE measurement. All experiments were carried out at room temperature (~22 °C).

The surface loading of the catalyst was calculated through the integration of the reoxidation wave in the CV scans

$$\Gamma_{Mn} = \frac{q}{nFA}$$

where Γ_{Mn} is the surface loading (mol cm^{-2}), q is the charge (C) obtained from integration of the oxidation wave, n the number of electrons in the redox process per Mn center (n = 1), F is the Faraday constant (96485 C mol^{-1}), and A is the geometrical electrode area (0.2 cm^2).

To model the impact of the $\mathbf{Mn_{pyr}}$ solution concentration over the surface loading, a single Langmuir isotherm was used

$$\Gamma_{Mn,eq} = \frac{\Gamma_{Mn,max} K_{Mn}[\mathbf{Mn_{pyr}}]}{1 + K_{Mn}[\mathbf{Mn_{pyr}}]}$$

where $\Gamma_{Mn,eq}$ is the equilibrium surface coverage of $\mathbf{Mn_{pyr}}$ (mol cm^{-2}), $\Gamma_{Mn,max}$ is the saturation surface coverage (mol cm^{-2}), and K_{Mn} (L mol^{-1}) the association constant of $\mathbf{Mn_{pyr}}$ with the MWCNT surface in DMF at room temperature.

UV−Vis SEC. Measurements were carried out using a Varian Cary 50 Bio UV−visible spectrometer. The measurements were performed using a three-electrode configuration using a Ag/AgCl (sat. KCl) reference electrode and platinum mesh as a counter electrode in a flat custom-designed three-necked electrochemical cell suited for UV−vis measurements. The working MWCNT-FTO electrode was placed between the beam source (FTO was not in contact with the solution to prevent degradation) and the collector to measure UV−vis spectra of the immobilized catalyst at different potentials.

ATR IR SEC. Surface-sensitive IR measurements were carried out in 60° single-reflection ATR configuration using an ATR-active Si prism and an IFS66v/s FT-IR spectrometer (Bruker Instruments) equipped with a photoconductive nitrogen-cooled MCT detector. A total of 400 scans were co-added for a spectrum. The spectral region was set to a range from 400 to 4000 cm^{-1}. The resolution of the spectra was 4 cm^{-1}. The MWCNT membrane film-coated Si prism was mounted into a homemade ATR IR spectroelectrochemical cell (fill volume of 5 mL).[85] The solvent-accessible electrode surface had a geometrical area of 0.9 cm^2. A Ag/AgCl 3 M KCl (DriRef, WPI) and a hydrogen flame-cleaned Pt wire (99%, Goodfellow) were used as reference and counter electrodes, respectively. All measurements were carried about at room temperature. Potentials were applied using an Autolab PGSTAT 12 (Metrohm) potentiostat. All measurements were carried out with either Ar or CO_2 overpressure. Absorbance (A) spectra were generated according to Lambert−Beer's equation

DOI: 10.1021/jacs.7b06269
J. Am. Chem. Soc. 2017, 139, 14425−14435

$$-\log \frac{I_{sample}}{I_{ref}} = A$$

I_{sample} denotes the relevant sample spectrum and I_{ref} the respective reference spectrum.

The normalized band intensities I_{band} as a function of applied electrode potential E were fitted using a transformed Nernst equation

$$I_{band} = \frac{1}{1 + e^{[(nF/RT)(E-E^{0\prime})]}} + C$$

I_{band} denotes the (normalized) intensity of the respective band. F, R, and T denote the Faraday constant, the ideal gas constant, and room temperature, respectively. n and $E^{0\prime}$ represent the number of transferred electrons and the apparent midpoint potential of the redox transition, respectively. Both values are varied in the fits. C is a dimensionless parameter, accounting for possible offsets to obtain better fits of the equation to the data set. Band fitting of the difference IR spectra was performed using a homemade software (Qpipsi).

Isotopic Labeling. CPE experiments were performed in a gastight single-compartment (for ^{13}CO detection) or two-compartment (for ^{13}C formate detection) electrochemical cell equipped with a CNT| $\mathbf{Mn_{pyr}}$ working electrode, Pt counter electrode, and Ag/AgCl (sat. KCl) reference electrode in phosphate buffer (0.1 M, pH 7). The solution was purged with N_2 for 10 min before the headspace gas was replaced with $^{12}CO_2$ or $^{13}CO_2$ (>99 atom % ^{13}C, Sigma-Aldrich) by evacuating three times and refilling with the respective CO_2 isotopologue. CPE was performed at $E_{appl} = -1.1$ V vs SHE for 3 and 12 h for CO and $HCOO^-$ detection, respectively. Subsequently, the headspace gas was transferred to an evacuated gas IR cell (SpecAc, 10 cm path length, equipped with KBr windows), and a high-resolution transmission FT-IR spectrum was collected on a Thermo Scientific Nicolet iS50 FT-IR spectrometer. For $H^{13}COO^-$ or $H^{12}COO^-$ detection, 35 μL of D_2O were added to 700 μL of the electrolyte solution in an NMR tube. The spectra were recorded on a Bruker DPX-400 MHz spectrometer at room temperature, and water suppression was applied.

Product Analysis. The amount of H_2 and CO produced during CPE measurements under N_2 or CO_2 (with 2% CH_4 as an internal standard) was quantified by gas chromatography by analyzing a 50 μL volume of the working electrode headspace compartment with a Shimadzu Tracera GC-2010 Plus using a barrier discharge ionization detector (BID). The gas chromatograph was equipped with a ShinCarbon micro ST column (0.53 mm diameter) kept at 40 °C, using helium carrier gas. $HCOO^-$ was analyzed by ion chromatography (Metrohm 882 compact IC plus ion chromatography system) with carbonate buffer (4 mM, pH 7.4) eluent containing acetone (50 mL L^{-1}). The Faradaic yield for H_2 and CO was calculated using

$$\text{Faradaic yield product (\%)} = 100 \times \frac{(2F \times n_{prod.})}{Q}$$

where F is the Faraday constant (C mol^{-1}), n_{prod} (mol) is the amount of H_2/CO measured in the headspace, $HCOO^-$ in the electrolyte solution, and Q (C) is the charged passed during electrolysis.

The surface loading (from CV) and product quantification (from CPE) were determined from separate sets of experiments in triplicate. The error bars shown in the graphs are the standard deviation calculated as previously described.[86]

■ ASSOCIATED CONTENT

Supporting Information

The Supporting Information is available free of charge on the ACS Publications website at DOI: 10.1021/jacs.7b06269.

Supporting figures (PDF)

■ AUTHOR INFORMATION

Corresponding Author

*reisner@ch.cam.ac.uk

ORCID

Erwin Reisner: 0000-0002-7781-1616

Author Contributions

‡B.R. and K.H.L. contributed equally.

Notes

The authors declare no competing financial interest.

Additional data related to this publication are available at the University of Cambridge data repository (https://doi.org/10.17863/CAM.13194).

■ ACKNOWLEDGMENTS

This work was supported by the Christian Doppler Research Association (Austrian Federal Ministry of Science, Research and Economy and the National Foundation for Research, Technology and Development), the OMV Group, the EPSRC (DTA studentship for T.E.R.), the European Union's Horizon 2020 research and innovation program (Marie Sklodowska-Curie IF for K.H.L., GAN 701192), and an ERC Consolidator Grant "MatEnSAP" (GAN 682833). We thank Prof. Peter Hildebrandt for helpful discussions. I.Z. is indebted to the German Research Foundation (DFG) for financial support within the cluster of excellence EXC 314: Unifying concepts in catalysis, "UniCat".

■ REFERENCES

(1) Costentin, C.; Robert, M.; Savéant, J.-M. *Chem. Soc. Rev.* **2013**, *42*, 2423.

(2) Qiao, J.; Liu, Y.; Hong, F.; Zhang, J. *Chem. Soc. Rev.* **2014**, *43*, 631.

(3) Aresta, M.; Dibenedetto, A.; Angelini, A. *Chem. Rev.* **2014**, *114*, 1709.

(4) Kim, D.; Sakimoto, K. K.; Hong, D.; Yang, P. *Angew. Chem., Int. Ed.* **2015**, *54*, 3259.

(5) Robert, M. *ACS Energy Lett.* **2016**, *1*, 281.

(6) Benson, E. E.; Kubiak, C. P.; Sathrum, A. J.; Smieja, J. M. *Chem. Soc. Rev.* **2009**, *38*, 89.

(7) Yamazaki, Y.; Takeda, H.; Ishitani, O. *J. Photochem. Photobiol. C* **2015**, *25*, 106.

(8) Takeda, H.; Cometto, C.; Ishitani, O.; Robert, M. *ACS Catal.* **2017**, *7*, 70.

(9) Bonin, J.; Maurin, A.; Robert, M. *Coord. Chem. Rev.* **2017**, *334*, 184.

(10) Thoi, V. S.; Kornienko, N.; Margarit, C. G.; Yang, P.; Chang, C. J. *J. Am. Chem. Soc.* **2013**, *135*, 14413.

(11) Chen, L.; Guo, Z.; Wei, X.-G.; Gallenkamp, C.; Bonin, J.; Anxolabéhère-Mallart, E.; Lau, K.-C.; Lau, T.-C.; Robert, M. *J. Am. Chem. Soc.* **2015**, *137*, 10918.

(12) Bourrez, M.; Orio, M.; Molton, F.; Vezin, H.; Duboc, C.; Deronzier, A.; Chardon-Noblat, S. *Angew. Chem., Int. Ed.* **2014**, *53*, 240.

(13) Sampson, M. D.; Nguyen, A. D.; Grice, K. A.; Moore, C. E.; Rheingold, A. L.; Kubiak, C. P. *J. Am. Chem. Soc.* **2014**, *136*, 5460.

(14) Hawecker, J.; Lehn, J.-M.; Ziessel, R. *J. Chem. Soc., Chem. Commun.* **1984**, 328.

(15) Keith, J. A.; Grice, K. A.; Kubiak, C. P.; Carter, E. A. *J. Am. Chem. Soc.* **2013**, *135*, 15823.

(16) Morimoto, T.; Nakajima, T.; Sawa, S.; Nakanishi, R.; Imori, D.; Ishitani, O. *J. Am. Chem. Soc.* **2013**, *135*, 16825.

(17) Windle, C. D.; Pastor, E.; Reynal, A.; Whitwood, A. C.; Vaynzof, Y.; Durrant, J. R.; Perutz, R. N.; Reisner, E. *Chem. - Eur. J.* **2015**, *21*, 3746.

(18) Chardon-Noblat, S.; Collomb-Dunand-Sauthier, M.-N.; Deronzier, A.; Ziessel, R.; Zsoldos, D. *Inorg. Chem.* **1994**, *33*, 4410.

(19) Kang, P.; Chen, Z.; Nayak, A.; Zhang, S.; Meyer, T. J. *Energy Environ. Sci.* **2014**, *7*, 4007.

(20) Kang, P.; Cheng, C.; Chen, Z.; Schauer, C. K.; Meyer, T. J.; Brookhart, M. *J. Am. Chem. Soc.* **2012**, *134*, 5500.
(21) Beley, M.; Collin, J.-P.; Ruppert, R.; Sauvage, J.-P. *J. Am. Chem. Soc.* **1986**, *108*, 7461.
(22) Chen, L.; Chen, G.; Leung, C.-F.; Yiu, S.-M.; Ko, C.-C.; Anxolabéhère-Mallart, E.; Robert, M.; Lau, T.-C. *ACS Catal.* **2015**, *5*, 356.
(23) Kuehnel, M. F.; Orchard, K. L.; Dalle, K. E.; Reisner, E. *J. Am. Chem. Soc.* **2017**, *139*, 7217.
(24) Lacy, D. C.; McCrory, C. C. L.; Peters, J. C. *Inorg. Chem.* **2014**, *53*, 4980.
(25) Chan, S. L.-F.; Lam, T. L.; Yang, C.; Yan, S.-C.; Cheng, N. M. *Chem. Commun.* **2015**, *51*, 7799.
(26) Chapovetsky, A.; Do, T. H.; Haiges, R.; Takase, M. K.; Marinescu, S. C. *J. Am. Chem. Soc.* **2016**, *138*, 5765.
(27) Zhang, X.; Wu, Z.; Zhang, X.; Li, L.; Li, Y.; Xu, H.; Li, X.; Yu, X.; Zhang, Z.; Liang, Y.; Wang, H. *Nat. Commun.* **2017**, *8*, 14675.
(28) Costentin, C.; Drouet, S.; Robert, M.; Savéant, J.-M. *Science* **2012**, *338*, 90.
(29) Rosas-Hernández, A.; Alsabeh, P. G.; Barsch, E.; Junge, H.; Ludwig, R.; Beller, M. *Chem. Commun.* **2016**, *52*, 8393.
(30) Bourrez, M.; Molton, F.; Chardon-Noblat, S.; Deronzier, A. *Angew. Chem., Int. Ed.* **2011**, *50*, 9903.
(31) Sampson, M. D.; Kubiak, C. P. *J. Am. Chem. Soc.* **2016**, *138*, 1386.
(32) Machan, C. W.; Kubiak, C. P. *Dalton Trans.* **2016**, *45*, 17179.
(33) Rosser, T. E.; Windle, C. D.; Reisner, E. *Angew. Chem., Int. Ed.* **2016**, *55*, 7388.
(34) Elgrishi, N.; Griveau, S.; Chambers, M. B.; Bedioui, F.; Fontecave, M. *Chem. Commun.* **2015**, *51*, 2995.
(35) Neri, G.; Walsh, J. J.; Wilson, C.; Reynal, A.; Lim, J. Y. C.; Li, X.; White, A. J. P.; Long, N. J.; Durrant, J. R.; Cowan, A. J. *Phys. Chem. Chem. Phys.* **2015**, *17*, 1562.
(36) Kramer, W. W.; McCrory, C. C. L. *Chem. Sci.* **2016**, *7*, 2506.
(37) Lin, S.; Diercks, C. S.; Zhang, Y.-B.; Kornienko, N.; Nichols, E. M.; Zhao, Y.; Paris, A. R.; Kim, D.; Yang, P.; Yaghi, O. M.; Chang, C. J. *Science* **2015**, *349*, 1208.
(38) Maurin, A.; Robert, M. *Chem. Commun.* **2016**, *52*, 12084.
(39) Walsh, J. J.; Neri, G.; Smith, C. L.; Cowan, A. J. *Chem. Commun.* **2014**, *50*, 12698.
(40) Rosser, T. E.; Reisner, E. *ACS Catal.* **2017**, *7*, 3131.
(41) Bullock, R. M.; Das, A. K.; Appel, A. M. *Chem. - Eur. J.* **2017**, *23*, 7626.
(42) Le Goff, A.; Artero, V.; Jousselme, B.; Tran, P. D.; Guillet, N.; Métayé, R.; Fihri, A.; Palacin, S.; Fontecave, M. *Science* **2009**, *326*, 1384.
(43) Elouarzaki, K.; Le Goff, A.; Holzinger, M.; Thery, J.; Cosnier, S. *J. Am. Chem. Soc.* **2012**, *134*, 14078.
(44) Wei, P.-J.; Yu, G.-Q.; Naruta, Y.; Liu, J.-G. *Angew. Chem., Int. Ed.* **2014**, *53*, 6659.
(45) Aoi, S.; Mase, K.; Ohkubo, K.; Fukuzumi, S. *Chem. Commun.* **2015**, *51*, 10226.
(46) De Volder, M. F. L.; Tawfick, S. H.; Baughman, R. H.; Hart, A. J. *Science* **2013**, *339*, 535.
(47) Karousis, N.; Tagmatarchis, N.; Tasis, D. *Chem. Rev.* **2010**, *110*, 5366.
(48) Li, F.; Zhang, B.; Li, X.; Jiang, Y.; Chen, L.; Li, Y.; Sun, L. *Angew. Chem., Int. Ed.* **2011**, *50*, 12276.
(49) Tran, P. D.; Le Goff, A.; Heidkamp, J.; Jousselme, B.; Guillet, N.; Palacin, S.; Dau, H.; Fontecave, M.; Artero, V. *Angew. Chem., Int. Ed.* **2011**, *50*, 1371.
(50) Gentil, S.; Serre, D.; Philouze, C.; Holzinger, M.; Thomas, F.; Le Goff, A. *Angew. Chem., Int. Ed.* **2016**, *55*, 2517.
(51) Reuillard, B.; Warnan, J.; Leung, J. J.; Wakerley, D. W.; Reisner, E. *Angew. Chem., Int. Ed.* **2016**, *55*, 3952.
(52) Blakemore, J. D.; Gupta, A.; Warren, J. J.; Brunschwig, B. S.; Gray, H. B. *J. Am. Chem. Soc.* **2013**, *135*, 18288.
(53) Kang, P.; Zhang, S.; Meyer, T. J.; Brookhart, M. *Angew. Chem., Int. Ed.* **2014**, *53*, 8709.
(54) Maurin, A.; Robert, M. *J. Am. Chem. Soc.* **2016**, *138*, 2492.
(55) Franco, F.; Cometto, C.; Ferrero Vallana, F.; Sordello, F.; Priola, E.; Minero, C.; Nervi, C.; Gobetto, R. *Chem. Commun.* **2014**, *50*, 14670.
(56) Smieja, J. M.; Sampson, M. D.; Grice, K. A.; Benson, E. E.; Froehlich, J. D.; Kubiak, C. P. *Inorg. Chem.* **2013**, *52*, 2484.
(57) Fei, H.; Sampson, M. D.; Lee, Y.; Kubiak, C. P.; Cohen, S. M. *Inorg. Chem.* **2015**, *54*, 6821.
(58) Agarwal, J.; Shaw, T. W.; Schaefer, H. F.; Bocarsly, A. B. *Inorg. Chem.* **2015**, *54*, 5285.
(59) Takeda, H.; Koizumi, H.; Okamoto, K.; Ishitani, O. *Chem. Commun.* **2014**, *50*, 1491.
(60) Ngo, K. T.; McKinnon, M.; Mahanti, B.; Narayanan, R.; Grills, D. C.; Ertem, M. Z.; Rochford, J. *J. Am. Chem. Soc.* **2017**, *139*, 2604.
(61) Franco, F.; Cometto, C.; Nencini, L.; Barolo, C.; Sordello, F.; Minero, C.; Fiedler, J.; Robert, M.; Gobetto, R.; Nervi, C. *Chem. - Eur. J.* **2017**, *23*, 4782.
(62) Walsh, J. J.; Smith, C. L.; Neri, G.; Whitehead, G. F. S.; Robertson, C. M.; Cowan, A. J. *Faraday Discuss.* **2015**, *183*, 147.
(63) Torralba-Peñalver, E.; Luo, Y.; Compain, J.-D.; Chardon-Noblat, S.; Fabre, B. *ACS Catal.* **2015**, *5*, 6138.
(64) Cheung, P. L.; Machan, C. W.; Malkhasian, A. Y. S.; Agarwal, J.; Kubiak, C. P. *Inorg. Chem.* **2016**, *55*, 3192.
(65) Lalaoui, N.; Reuillard, B.; Philouze, C.; Holzinger, M.; Cosnier, S.; Le Goff, A. *Organometallics* **2016**, *35*, 2987.
(66) Reuillard, B.; Le Goff, A.; Cosnier, S. *Chem. Commun.* **2014**, *50*, 11731.
(67) Costentin, C.; Robert, M.; Savéant, J.-M. *Acc. Chem. Res.* **2015**, *48*, 2996.
(68) Artero, V.; Fontecave, M. *Chem. Soc. Rev.* **2013**, *42*, 2338.
(69) Kornienko, N.; Zhao, Y.; Kley, C. S.; Zhu, C.; Kim, D.; Lin, S.; Chang, C. J.; Yaghi, O. M.; Yang, P. *J. Am. Chem. Soc.* **2015**, *137*, 14129.
(70) Zhu, D. D.; Liu, J. L.; Qiao, S. Z. *Adv. Mater.* **2016**, *28*, 3423.
(71) Balland, V.; Lecomte, S.; Limoges, B. *Langmuir* **2009**, *25*, 6532.
(72) Abel, E. W.; Stone, F. G. A. *Q. Rev., Chem. Soc.* **1969**, *23*, 325.
(73) Hartl, F.; Mahabiersing, T.; Le Floch, P.; Mathey, F.; Ricard, L.; Rosa, P.; Záliš, S. *Inorg. Chem.* **2003**, *42*, 4442.
(74) Healy, A. J.; Ash, P. A.; Lenz, O.; Vincent, K. A. *Phys. Chem. Chem. Phys.* **2013**, *15*, 7055.
(75) Wisitruangsakul, N.; Lenz, O.; Ludwig, M.; Friedrich, B.; Lendzian, F.; Hildebrandt, P.; Zebger, I. *Angew. Chem., Int. Ed.* **2009**, *48*, 611.
(76) Millo, D.; Hildebrandt, P.; Pandelia, M.-E.; Lubitz, W.; Zebger, I. *Angew. Chem., Int. Ed.* **2011**, *50*, 2632.
(77) Baruch, M. F.; Pander, J. E., III; White, J. L.; Bocarsly, A. B. *ACS Catal.* **2015**, *5*, 3148.
(78) Dunwell, M.; Lu, Q.; Heyes, J. M.; Rosen, J.; Chen, J. G.; Yan, Y.; Jiao, F.; Xu, B. *J. Am. Chem. Soc.* **2017**, *139*, 3774.
(79) Ly, H. K.; Wrzolek, P.; Heidary, N.; Götz, R.; Horch, M.; Kozuch, J.; Schwalbe, M.; Weidinger, I. M. *Chem. Sci.* **2015**, *6*, 6999.
(80) Rodriguez-Maciá, P.; Dutta, A.; Lubitz, W.; Shaw, W. J.; Rüdiger, O. *Angew. Chem., Int. Ed.* **2015**, *54*, 12303.
(81) Splinter, R.; Hooper, B. A. *An Introduction to Biomedical Optics*; Taylor & Francis: Hoboken, NJ, 2006.
(82) Paoloni, L.; Patti, A.; Mangano, F. *J. Mol. Struct.* **1975**, *27*, 123.
(83) Zaragoza-Galán, G.; Fowler, M. A.; Duhamel, J.; Rein, R.; Solladié, N.; Rivera, E. *Langmuir* **2012**, *28*, 11195.
(84) Wu, Z.; Chen, Z.; Du, X.; Logan, J. M.; Sippel, J.; Nikolou, M.; Kamaras, K.; Reynolds, J. R.; Tanner, D. B.; Hebard, A. F.; Rinzler, A. G. *Science* **2004**, *305*, 1273.
(85) Wisitruangsakul, N.; Zebger, I.; Ly, K. H.; Murgida, D. H.; Ekgasit, S.; Hildebrandt, P. *Phys. Chem. Chem. Phys.* **2008**, *10*, 5276.
(86) Gross, M. A.; Reynal, A.; Durrant, J. R.; Reisner, E. *J. Am. Chem. Soc.* **2014**, *136*, 356.

DOI: 10.1021/jacs.7b06269
J. Am. Chem. Soc. 2017, 139, 14425−14435